# Towards a Multiscale Scheme for Nonlinear Dynamic Analysis of Masonry Structures with Damage

**Savvas P. Triantafyllou and Eleni N. Chatzi**

**Abstract** In this work, a three dimensional multiscale formulation is presented for the analysis of masonry structures based on the multiscale finite element formulation. The method is developed within the framework of the Enhanced Multiscale Finite Element Method. Through this approach, two discretization schemes are considered, namely a fine mesh that accounts for the micro-structure and a coarse mesh that encapsulates the former. Through a numerically derived mapping, the fine scale information is propagated to the coarse mesh where the numerical solution of the governing equations is performed. Inelasticity is introduced at the fine mesh by considering a set of internal variables corresponding to the plastic deformation accumulating at the Gauss points of each fine-scale element. These additional quantities evolve according to properly defined smooth evolution equations. The proposed formalism results in a nonlinear dynamic analysis method where the micro-level state matrices need only be evaluated once at the beginning of the analysis procedure. The accuracy and computational efficiency of the proposed scheme is verified through an illustrative example.

**Keywords** Multiscale analysis · Hysteresis · Masonry · Textile reinforcement

S.P. Triantafyllou (✉)
Department of Civil Engineering, The University of Nottingham, University Park, Nottingham NG7 2RD, UK
e-mail: savvas.triantafyllou@nottingham.ac.uk

E.N. Chatzi
Institute of Structural Engineering, ETH, Stefano-Franscini-Platz 5, 8093 Zurich, Switzerland
e-mail: chatzi@ibk.baug.ethz.ch



I.N. Psycharis et al. (eds.), *Seismic Assessment, Behavior and Retrofit of Heritage Buildings and Monuments*, Computational Methods in Applied Sciences 37, DOI 10.1007/978-3-319-16130-3_7

## 1 Introduction

Masonry structures constitute a large portion of the existing building stock and in many cases involve buildings of significant social and cultural importance. With rare exceptions, masonry buildings in historic urban settlements have been conceived only for gravity loads. Unreinforced masonry constructions are amongst the classes of structures severely harmed during earthquake events. Even in cases where some sort of aseismic structural system has been devised, its performance over the course of years tends to deteriorate. The recent seismic events of Modena, 2012, Christchurch 2011, L Aquila, 2009 tragically pointed out the need for restoration and reinforcement of existing masonry buildings not only for the conservation of cultural heritance but also for the protection of human lives [1, 2]. Failures have been also documented that are not directly related to seismic events rather to long term damage accumulation. Such examples are the Civic Tower at Pavia in Italy, 1989 [3] and more recently the collapse of the bell tower of the St. Willibrordus Church at Meldert, Belgium and the partial collapse of the Medieval Maagden tower at Zichem, Belgium [4].

Within this framework, polymeric materials in the form of sheets [5], distributed reinforcing fibers [6] and multi-functional textiles [7], are extensively used for the retrofitting and strengthening of existing or newly built infrastructure [8]. In implementations pertaining to preservation of architectural heritage, including masonry and historic structures, polymeric solutions are becoming increasingly popular [9, 10] since they comprise reversible interventions that do not adversely affect the character of the structure or monument. In recent years, textile solutions in particular are gaining ground as they provide a minimally intrusive means for recovering structural strength, improving structural performance under service conditions and additionally provide protection in the event of an extreme event [7, 11]. On a step further the embedment of sensors in such textile solutions may provide valuable information for characterising such complex materials [12, 13].

Masonry is a composite material comprising distinct units of various natural or industrial materials e.g. stone, brick, concrete etc. [14]. Individual units are split by joints that can be either filled with mortar or not. In most cases, the mechanical properties of the units exhibit severe anisotropy, which is correspondingly reflected in the mechanical properties of the composite. This anisotropy is further affected by the mechanical properties of the mortar. Thus, a masonry wall demonstrates different values of bending strength when in-plane or out-of plane bending is considered [15]. Furthermore, the various construction techniques implemented also lead to severe variations on the masonry mechanical properties as in the case of multi-leaf masonry systems [16].

To assess the structural integrity of an existing masonry structure and also design and predict the performance of a retrofitted structure, the engineer needs to account for this intricate material and structural behaviour. Modern design codes [17, 18]

provide guidance for the assessment of existing and retrofitted structures within the framework of performance based design [19]. In this, the nonlinear response of the structure is evaluated and its integrity is verified with respect to predefined levels of structural performance. On practice, the evaluation of the structural response is performed through a series of nonlinear static analysis procedures. Although nonlinear dynamic analysis procedures provide a more thorough and exact estimation of the actual response, both the increased computational cost of a nonlinear analysis procedure as well as the large amount of output data that usually needs to be processed (i.e. of the order of GBs) renders its application prohibitive for the design office.

Nonlinear modeling of masonry is a difficult and challenging task due to the inherent complexities concerning the nonlinear behaviour of either the constituent materials (stone and mortar) or the resulting structural system. Masonry materials usually demonstrate a brittle and in general anisotropic behaviour in the micro-level. The anisotropy at the micro level together with the inherent weak directions (along the head and bed joints) results in a highly anisotropic macroscopic behaviour [20, 21]. The computational methods used for the nonlinear analysis of masonry structures are classified into three main categories, namely macro-scale, micro-scale and multi-scale methods [22]. Macro-models commonly pertain to orthotropic materials with different tensile and compressive strengths along the material axes. Furthermore, different inelastic properties for each material axis have to be reproduced. A reduced number of orthotropic material models specific for masonry have been proposed [23]. Recently in [24] a macro-element has been presented for the nonlinear analysis of unreinforced masonry piers considering only the in-plane structural response. In general, macro-modeling is a fast and reliable analysis tool when the qualitative response of a structure is sought. However the accuracy of the method significantly depends on the generalized material properties used and the corresponding assumptions made on the governing parameters of the problem. These are not easy to identify and the use of finer methods is necessary either to get accurate results or to correctly specify the macro-modeling material parameters.

Micro-modeling approaches comprise refined masonry models employing a distinct representation of units, mortar and the unit/mortar interface. In this case, continuum elements are used to represent units and mortar in the joints whereas the unit-mortar interface is modelled via discontinuous elements which account for potential crack/slip planes. Though exact, this modeling approach leads to large memory and computational time requirements.

To further enhance the computational efficiency of micro-modeling techniques while retaining their level of refinement, multi-scale approaches have been introduced. Homogenization approaches are multi-scale modeling methods that rely on the definition of a Representative Volume Element (RVE) and the evaluation of average stress and strain measures over the RVE domain. Homogenization

approaches have been successfully implemented for the linear and nonlinear analysis of various heterogeneous materials. Recently, Massart et al. [20, 25, 26] have developed a meso-scale constitutive model for masonry that accounts for anisotropic plasticity effects and damage of the constituents implementing a generalized plane state assumption.

However these methods are based on two main assumptions i.e. scale separation within the RVE and periodicity of the RVE. The latter assumption poses a strict constraint on the geometrical domains that can be addressed through this method. Multiscale Finite Element methods (MsFEM) [27, 28] are based on the notion of nested finite element meshes, defined across different scales. On each mesh a corresponding displacement field is also defined. Based on a set of kinematic assumptions a numerically derived interpolation field is defined between the different scales that maps the micro to macro displacement field. While the micro-modeling properties are accounted for in the inner (or finer) finite element mesh, the solution of the governing equations is performed on the outer (or coarser) mesh at a significantly reduced computational cost. Recently the method has been extended to account for the nonlinear dynamic response of heterogeneous domains [29] using the hysteretic finite element method at the fine scale [30]. Using this approach, inelasticity is introduced at the fine scale by formulating the evolution equations of plastic deformation within the framework of classical plasticity [31].

In what follows, the hysteretic multiscale finite element method is used to assess the nonlinear dynamic response of masonry structures. A two-scale analysis approach is implemented. In the micro-scale, a fine-meshed finite element mesh is defined accounting for each different constituent material. Using the micro to macro interpolation scheme of MsFEM, the fine-scale is mapped at a coarser mesh where the solution of the governing equations of motion is performed at a significantly reduced computational cost. The nonlinear behaviour of the constituent materials is treated using a properly defined smooth hysteretic model. In this, inelasticity is treated within the framework of classical plasticity while damage is introduced through additional hysteretic variables that account for stiffness degradation, strength deterioration and pinching of the corresponding material.

The micro measures of the structural response (i.e. micro-displacements, micro-stresses and micro-strains) can be evaluated through the inverse micro to macro mapping procedure. Therefore, the amount of output data is also significantly reduced as these measures can be evaluated on demand during the post-processing phase of the analysis. In Sect. 2 the hysteretic model considered for the nonlinear behaviour at the constituent level is described. In Sect. 3 the EMsFE method is presented while the proposed hysteretic multiscale formulation is described in Sect. 4. Finally, the application of the method for the analysis of masonry structures is described in Sects. 5 and 6. In Sect. 5, the response at the material level is examined. In Sect. 6, the dynamic response of a natural stone masonry wall under earthquake excitation is examined with and without textile composite reinforcement.

## 2 Smooth Hysteretic Modeling

### 2.1 From Classical Plasticity to Smooth Hysteretic Modeling

The hysteretic formulation of finite elements [30] is implemented herein to account for the nonlinear dynamic behaviour of materials at the micro-scale. In this, a mixed interpolation scheme is considered for both the displacement and the plastic component of the strain tensor. The method is based on the additive decomposition of the strain rates into a reversible elastic and an irreversible inelastic component [32] that is defined through the following relation:

$$\{\dot{\varepsilon}\} = \left\{\dot{\varepsilon}^{el}\right\} + \left\{\dot{\varepsilon}^{pl}\right\} \tag{1}$$

where $\{\varepsilon\}$ is the tensor of total strain, $\{\varepsilon^{el}\}$ is the tensor of the elastic, reversible, strain and $\{\varepsilon^{pl}\}$ is the tensor of the plastic strain. The vectorial notation of the stress and strain tensors is used in this work while the (.) symbol denotes differentiation with respect to time. In classical elasto-plasticity, the elastic component of the strain tensor $\{\varepsilon^{el}\}$ is directly related to the current stress $\{\sigma\}$ through the Hooke's law

$$\{\dot{\sigma}\} = [D]\left\{\dot{\varepsilon}^{el}\right\} \tag{2}$$

where $[D]$ is the elastic material constitutive matrix. Using relation (1), Eq. (2) is re-written in the following form

$$\{\dot{\sigma}\} = [D]\left(\{\dot{\varepsilon}\} - \left\{\dot{\varepsilon}^{pl}\right\}\right) \tag{3}$$

The evolution of the plastic part of the deformation component is defined through the flow rule

$$\left\{\dot{\varepsilon}^{pl}\right\} = \dot{\lambda}\frac{\partial \mathscr{F}}{\partial\{\sigma\}} \tag{4}$$

where $\mathscr{F}$ is the plastic potential [31]. Substituting relation (4) into Eq. (3) the following expression is retrieved

$$\{\dot{\sigma}\} = [D]\left(\{\dot{\varepsilon}\} - \dot{\lambda}\frac{\partial \mathscr{F}}{\partial\{\sigma\}}\right) \tag{5}$$

Elasticity is defined as the locus of points in the stress space lying in the interior of the yield surface, defined through the following relation

$$\Phi(\{\sigma\}, \{\eta\}) = 0 \tag{6}$$

where $\{\eta\}$ is the back-stress tensor whose evolution determines the motion of the yield surface in the stress-space.

The evolution of the back-stress tensor is determined by the kinematic hardening law that assumes the following form

$$\{\dot{\eta}\} = \dot{\lambda}\{\mathscr{G}\}_{kin}\left(\{\eta\}, \{\varepsilon^{pl}\}, \{\dot{\varepsilon}^{pl}\}\right) \tag{7}$$

where $\{\mathscr{G}\}_{kin}$ is the kinematic hardening function. The equivalent plastic strain $p$ is an appropriate measure of the accumulation of plastic deformation defined from the following relation

$$p = \int_0^t \sqrt{\frac{3}{2}\{\dot{\varepsilon}^{pl}\}^T\{\dot{\varepsilon}^{pl}\}}dt \tag{8}$$

Substituting Eq. (4) in Eq. (8), the following relation is established

$$p = \int_0^t \dot{\lambda}\sqrt{\frac{3}{2}\left\{\frac{\partial \mathscr{F}}{\partial\{\sigma\}}\right\}^T\left\{\frac{\partial \mathscr{F}}{\partial\{\sigma\}}\right\}}dt \tag{9}$$

Using the consistency condition of classical plasticity, the following relation is established

$$\dot{\Phi} = 0 \Rightarrow \left(\frac{\partial \Phi}{\partial\{\sigma\}}\right)^T\{\dot{\sigma}\} + \left(\frac{\partial \Phi}{\partial\{\eta\}}\right)^T\{\dot{\eta}\} = 0 \tag{10}$$

Substituting relations (5) and (7) into (10) and solving $\dot{\lambda}$, the following relation is established

$$\dot{\lambda} = \kappa \underbrace{\left(\frac{\partial \Phi}{\partial\{\sigma\}}\right)^T}_{1x6} \overbrace{[D]}^{6x6} \underbrace{\{\dot{\varepsilon}\}}_{6x1} \tag{11}$$

where $\kappa$ is a scalar derived from the following relation

$$\kappa = \left( - \underbrace{\left(\frac{\partial \Phi}{\partial\{\eta\}}\right)^T}_{1x6} \overbrace{\{G_{kin}\}}^{6x1} + \underbrace{\left(\frac{\partial \Phi}{\partial\{\sigma\}}\right)^T}_{1x6} \overbrace{[D]}^{6x6} \underbrace{\frac{\partial \mathscr{F}}{\partial\{\sigma\}}}_{6x1} \right)^{-1} \tag{12}$$

Since the evolution of the plastic multiplier is defined on the grounds of the consistency condition (10), relation (11) is valid only at yield, i.e. when $\Phi = 0$. Introducing the following smooth Heaviside type functions, namely

$$H_1 = \left| \frac{\Phi(\{\sigma\}, \{\eta\}, R)}{\Phi_0} \right|^N, \quad N \geq 2 \tag{13}$$

and

$$H_2 = \beta + \gamma sgn\left(\dot{\Phi}\right) \tag{14}$$

relation (11) can be cast in the following convenient form

$$\dot{\lambda} = H_1 H_2 \kappa \underbrace{\left( \frac{\partial \Phi}{\partial \{\sigma\}} \right)^T}_{1x6} \overbrace{[D]}^{6x6} \underbrace{\{\dot{\varepsilon}\}}_{6x1} \tag{15}$$

Equation (15) governs the evolution of the plastic multiplier along the full loading-unloading-reloading cycle. When either $H_1$ or $H_2$ is equal to zero the elastic regime of the material response is retrieved whereas when both $H_1 = 1$ and $H_2 = 1$ plastic deformations accumulate.

Substituting relation (15) into Eq. (4) the following flow rule is retrieved

$$\left\{\dot{\varepsilon}^{pl}\right\} = H_1 H_2 [R] \{\dot{\varepsilon}\} \tag{16}$$

where $[R]$ is an interaction matrix defined as:

$$[R] = \kappa \underbrace{\left( \frac{\partial \Phi}{\partial \{\sigma\}} \right)}_{6x1} \underbrace{\left( \frac{\partial \Phi}{\partial \{\sigma\}} \right)^T}_{1x6} \overbrace{[D]}^{6x6} \tag{17}$$

Similarly, by substituting Eq. (15) into relation (7), the evolution of the back-stress tensor is derived as:

$$\{\dot{\eta}\} = H_1 H_2 \kappa \overbrace{\{\mathcal{G}_{kin}\}}^{6x1} \underbrace{\left( \frac{\partial \Phi}{\partial \{\sigma\}} \right)^T}_{1x6} \overbrace{[D]}^{6x6} \underbrace{\{\dot{\varepsilon}\}}_{6x1} \tag{18}$$

The derived model constitutes a generic smooth form of the classical plasticity framework and is fully defined by determining the expressions of the yield surface $\Phi$, the kinematic hardening function $\{\mathcal{G}\}_{kin}$ and the additional material parameters $N$, $\beta$ and $\gamma$.

## 2.2 Damage Induced Phenomena

In this work, stiffness degradation, strength deterioration and pinching are taken into account by introducing additional material parameters within the hysteretic finite element scheme. These parameters are accompanied by a set of corresponding evolution equations that depend on the hysteretic energy accumulated over time. The relations are based on the derivations introduced in [33, 34].

The stiffness degradation parameter is introduced at the stress-strain relation (2), which assumes the following form

$$\{\dot{\sigma}\} = v_\eta [D] \left\{\dot{\varepsilon}^{el}\right\} \tag{19}$$

where $v_\eta$ is a degradation parameter that is equal to unity as long as the material has not yielded and increases as a function of the plastic deformation. The following generic expression is thus defined:

$$\dot{v}_\eta = \mathcal{K}_\eta (E_h) \tag{20}$$

where $E_h$ is the hysteretic energy of the $i$th micro-element.

Solving Eq. (1) for $\left\{\dot{\varepsilon}^{el}\right\}$ and substituting into Eq. (19) the following relation is finally derived:

$$\{\dot{\sigma}\} = v_\eta [D] \left(\{\dot{\varepsilon}\} - \left\{\dot{\varepsilon}^{pl}\right\}\right) \tag{21}$$

where the total stress tensor is expressed as a function of the total and plastic strain tensors and the degradation parameter. For the purpose of this work, a constant rate stiffness degradation rule is considered and thus relation (20) is expressed as

$$\left.\begin{array}{l} \dot{v_\eta} = C_s \\ v_\eta\big|_{E_h=0} = 1.0 \end{array}\right\} \Rightarrow v_\eta = 1.0 + c_\eta E_h \tag{22}$$

where $\eta_{sd}$ is a material parameter.

Strength deterioration is accounted for by introducing parameter $v_s$ into the yield related smooth Heaviside function $H_1$ defined in relation (13)

$$H_1 = \left| v_s \frac{\Phi(\{\sigma\}, \{\eta\}, R)}{\Phi_0} \right|^N, \quad N \geq 2 \tag{23}$$

where in general $v_s$ is a function of the hysteretic energy accumulated within the element

$$\dot{v}_s = \mathcal{K}_v (E_h) \tag{24}$$

A constant rate evolution law is also considered in this work, thus the variation of the strength deterioration parameter $v_s$ is defined as

$$\left.\begin{array}{c} \dot{v_s} = c_s \\ v_s|_{E_h=0} = 1.0 \end{array}\right\} \Rightarrow v_s = 1.0 + c_s E_h \tag{25}$$

where $c_s$ is a user defined material parameter.

Finally pinching is defined on the basis of the pinching parameter $h_p$ that is directly introduced in the stress-strain relation (21)

$$\{\dot{\sigma}\} = \frac{v_\eta}{h_p}[D]\left(\{\dot{\varepsilon}\} - \left\{\dot{\varepsilon}^{pl}\right\}\right) \tag{26}$$

The corresponding evolution equation is defined as

$$h_p = 1 - \zeta_1 e^{-\left(H_1 sign\left(\dot{\Phi}\right) - q/v_s\right)^2/\zeta_2^2} \tag{27}$$

where $q$ is a material constant. Variables $\zeta_1$ and $\zeta_2$ are defined as

$$\zeta_1 = \zeta_1^0\left(1 - e^{-pE_h}\right) \tag{28}$$

and

$$\zeta_2 = \left(\psi_0 + \delta_\psi E_h\right)(\mu + \zeta_1) \tag{29}$$

where $\zeta_1^0$, $p$, $\psi_0$, $\delta_\psi$ and $\mu$ are also material constants.

## 3 The Enhanced Multiscale Finite Element Analysis Method

In this section, the Enhanced Multiscale Finite Element Method (EMsFEM) is briefly outlined for reasons of completeness and for serving as a reference for subsequent derivations. A masonry frame is presented in Fig. 1, consisting of two piers and a horizontal spandrel. An additional outer layer of reinforcement is also considered. The computational fine scale model consists of 8-node hex elements [35]. Instead of directly solving the fine scale computational model using the standard isoparametric finite element formulation, EMsFEM is based on a two-step approach. Grouping together clusters of micro-elements, a set of coarse elements is constructed. The nodes of the derived macro-elements are the macro-nodes of the coarse mesh. Accordingly, two displacement fields are defined, namely the micro-displacement field corresponding to the micro nodal displacements $\{\, u_m(x,y) \quad v_m(x,y) \quad w_m(x,y) \,\}^T$ of the fine mesh and the macro-displacement field $\{\, u_M(x,y) \quad v_M(x,y) \quad w_M(x,y) \,\}^T$

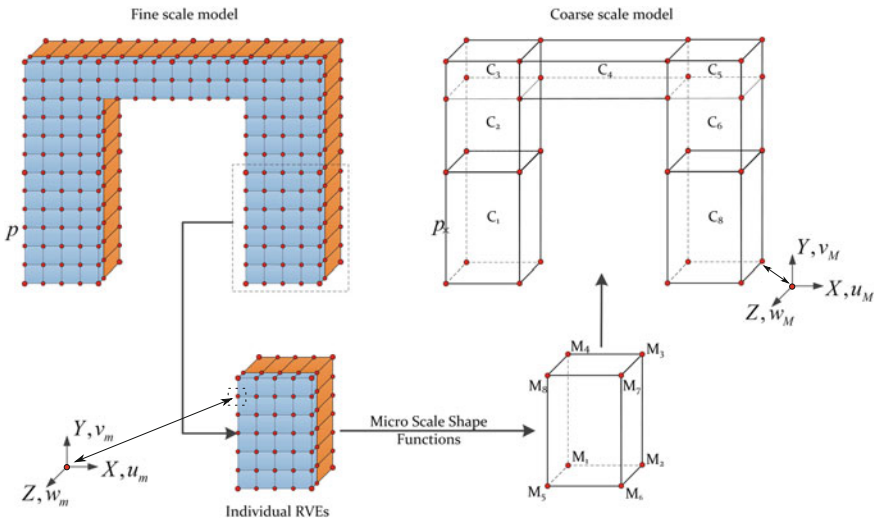


**Fig. 1** Multiscale finite element procedure

corresponding to the macro nodal displacements. Throughout this work, subscript $m$ denotes a micro-measure while $M$ is used to denote a macro-measure of the indexed quantity.

Next, a numerical mapping is constructed that maps the micro-displacement field within each RVE to the corresponding macro-displacements of the RVE macro-nodes. This numerical mapping assumes the following generic form:

$$\{d\}_m = \mathscr{M}\{d\}_M \tag{30}$$

where $\mathscr{M}$ is a mapping operator. EMsFEM is based on the assumption that the discrete micro-displacements within the coarse element are interpolated at the macro-nodes using the following scheme:

$$u_m(x_j, y_j) = \sum_{i=1}^{n_{Macro}} N_{ijxx} u_{M_i} + \sum_{i=1}^{n_{Macro}} N_{ijxy} v_{M_i} + \sum_{i=1}^{n_{Macro}} N_{ijxz} w_{M_i} \tag{31}$$

$$v_m(x_j, y_j) = \sum_{i=1}^{n_{Macro}} N_{ijxy} u_{M_i} + \sum_{i=1}^{n_{Macro}} N_{ijyy} v_{M_i} + \sum_{i=1}^{n_{Macro}} N_{ijyz} w_{M_i} \tag{32}$$

$$w_m(x_j, y_j) = \sum_{i=1}^{n_{Macro}} N_{ijxz} u_{M_i} + \sum_{i=1}^{n_{Macro}} N_{ijyz} v_{M_i} + \sum_{i=1}^{n_{Macro}} N_{ijzz} w_{M_i} \tag{33}$$

where $j = 1 \ldots n_{micro}$ is the jth micro-node, $u_m$, $v_m$, $w_m$ are the horizontal and vertical micro-displacement components, $n_{Macro}$ is the number of macro-nodes of the coarse element, $(x_j, y_j, z_j)$ are the local coordinates of the micro-nodes, $u_{M_i}$, $v_{M_i}$, $w_{M_i}$ are the

horizontal and vertical displacement components of the macro-nodes, $N_{ixx}$, $N_{ixy}$, $N_{iyy}$, $N_{iyz}$, $N_{izz}$ are the micro-basis functions and $n_{micro}$ is the number of micro-nodes within the coarse element.

In Eqs. (31)–(33), $N_{ijxx}$ stands for the displacement component of node $j$ along the $x$ axis induced by a unilateral displacement at the $i$th node (also along the $x$ axis). Likewise, $N_{ijxy}$ stands for the displacement component of the $i$th node, along the $x$ axis induced by a unilateral displacement at node $j$ and along the $y$ axis. Contrary to MsFEM where the interpolation fields of the displacement components are considered uncoupled, the coupling terms $N_{ixy}$, $N_{ixz}$, $N_{iyz}$ are introduced in EMsFEM. Thus, Eqs. (31)–(33) result in a kinematical assumption consistent with the observation that a unit displacement in the boundary of a deformable body may induce displacements in both directions within the body.

From the interpolation field introduced in Eqs. (31)–(33), the following relation can be established at the micro-elemental level

$$\{d\}_{m(i)} = [N]_{m(i)} \{d\}_M \tag{34}$$

where $\{d\}_{m(i)}$ is the nodal displacement vector of the $i$th micro-element, $[N]_{m(i)}$ is a matrix containing the micro-basis shape functions evaluated at the nodes of the $i$th micro-element while $\{d\}_M$ the vector of nodal displacements of the corresponding macro-nodes.

## 3.1 Numerical Evaluation of Micro-scale Basis Functions

The evaluation of the mapping operator $\mathscr{M}$ is performed numerically. Relations (31)–(33) successfully map the micro-displacement field to the macro-displacement field if and only if the micro-shape functions adhere to the following property, namely, when the macro-displacement component is equal to unity at a macro-node, displacement is equal to zero at every other macro-node. The derivation of micro-basis functions with such properties can be accomplished by considering the following boundary value problem

$$\begin{aligned} [K]_{RVE}\{d\}_m &= \emptyset \\ \{d\}_S &= \{\bar{d}\} \end{aligned} \tag{35}$$

where $[K]_{RVE}$ is the stiffness matrix of the RVE, $\{\emptyset\}$ is a vector containing zeros while $\{d\}_S$ is a vector containing the nodal degrees of freedom of the boundary $S$ of the RVE and $\{\bar{d}\}$ is a vector of prescribed displacements. The RVE stiffness matrix is formulated using the standard finite element method [36]. In this work, the solution of the boundary value problem established in Eq. (35) is performed using the Penalty method [37].

The choice of the values of the prescribed boundary displacements is a key assumption of the EMsFEM and highly affects the accuracy of the derived multiscale scheme. Three different types of boundary conditions are established in the literature namely linear boundary conditions, oscillatory boundary conditions and oscillatory boundary conditions with oversampling. Further details on the procedure implemented for the derivation of the micro-basis functions can be found in [27, 28].

## 4 The Hysteretic Multiscale Finite Element Analysis Method

The hysteric approach for implementation within the context of multi scale dynamic analysis has recently been introduced by Triantafyllou and Chatzi [29]. The evaluation of the micro-shape functions for each RVE is based on the solution of the equilibrium problem (35). Thus, the mapping depends on the material properties of the fine-scale model, e.g. for the case of the reinforced masonry RVE presented in Fig. 1, the solution depends on the material properties of masonry and the composite matrix. Consequently, in a nonlinear analysis procedure, either static or dynamic, the evaluation of the micro to macro-mapping is performed in every incremental step of the analysis. To overcome this computational hurdle, the hysteretic formulation of finite elements is implemented [38] in this work, accounting for the nonlinear material behaviour in the fine scale.

The derivations presented herein are based on the additive decomposition of the micro strain rates into elastic and plastic parts defined in relation (1) which is rewritten here in the following form

$$\{\dot{\varepsilon}\}_{m(i)} = \left\{\dot{\varepsilon}^{el}\right\}_{m(i)} + \left\{\dot{\varepsilon}^{pl}\right\}_{m(i)} \tag{36}$$

where the index $m(i)$ denotes the corresponding measure of the $i$th micro-element.

The multi-scale formulation is based on the following variational formulation [39]

$$\int_{V_{m(i)}} \{\varepsilon\}^T_{m(i)} \{\dot{\sigma}\}_{m(i)} dV_{m(i)} = \{d\}^T_{m(i)} \{\dot{f}\}_{m(i)} \tag{37}$$

where $\{d\}_{m(i)}$ is the vector of micro-nodal displacements introduced in relation (34), $\{f\}_{m(i)}$ is the corresponding vector of nodal forces and where $V_{m(i)}$ is the volume of the $i$th micro-element. For the sake of the presentation, only nodal loads are considered herein, however the evaluation of body loads and surface tractions can be derived accordingly. Substituting Eq. (36) into the variational principle (37) the following relation is derived:

$$\int_{V_{m(i)}} \{\varepsilon\}_{m(i)}^T [D]_{m(i)} \{\dot{\varepsilon}\}_{m(i)} dV_e - \int_{V_e} \{\varepsilon\}_{m(i)}^T [D]_{m(i)} \left\{\dot{\varepsilon}^{pl}\right\}_{m(i)} dV_{m(i)} = \{d\}_{m(i)}^T \{\dot{f}\}_{m(i)} \tag{38}$$

Considering the standard isoparametric interpolation scheme [35] for the micro-displacement field $\{u\}_{m(i)}$

$$\{u\}_{m(i)} = [N]_{m(i)} \{d\}_{m(i)} \tag{39}$$

with the accompanying strain-displacement compatibility relation:

$$\{\varepsilon\}_{m(i)} = [B]_{m(i)} \{d\}_{m(i)} \tag{40}$$

where $[N]_{m(i)}$ is the matrix of shape functions for the 8-node solid element [35], and $[B]_{m(i)} = \partial [N]_{m(i)}$ is the corresponding strain-displacement matrix. Substituting Eq. (40) into Eq. (38) the following relation is derived:

$$\int_{V_e} [B]_{m(i)}^T [D]_{m(i)} [B]_{m(i)} dV_e \left\{\dot{d}\right\}_{m(i)} - \int_{V_e} [B]_{m(i)}^T [D]_{m(i)} \left\{\dot{\varepsilon}^{pl}\right\}_{m(i)} dV_e = \left\{\dot{f}\right\}_{m(i)} \tag{41}$$

Furthermore, introducing an interpolation scheme $[N_\sigma]_{m(i)}$ for the plastic part of the strain $\left\{\varepsilon^{pl}\right\}_{m(i)}$, namely:

$$\underbrace{\left\{\dot{\varepsilon}^{pl}\right\}_{m(i)}}_{6x1} = \underbrace{[N_\sigma]_{m(i)}}_{6x6n_{cq}} \overbrace{\left\{\dot{\varepsilon}_{cq}^{pl}\right\}_{m(i)}}^{6n_{cq}x1} \tag{42}$$

where $\left\{\varepsilon_{cq}^{pl}\right\}_{m(i)}$ is the vector of plastic stains retrieved at properly defined collocation points and $n_{cq}$ is the number of collocation points used, the following relation is finally derived:

$$\left[k^{el}\right]_{m(i)} \left\{\dot{d}\right\}_{m(i)} - \left[k^h\right]_{m(i)} \left\{\dot{\varepsilon}_{cq}^{pl}\right\}_{m(i)} = \left\{\dot{f}\right\}_{m(i)} \tag{43}$$

where $\left[k^{el}\right]_{m(i)}$ is the elastic stiffness matrix of the micro-element

$$\left[k^{el}\right]_{m(i)} = \int_{V_{m(i)}} [B]_{m(i)}^T [D]_{m(i)} [B]_{m(i)} dV_{m(i)} \tag{44}$$

and $\left[k^h\right]_{m(i)}$ is the hysteretic matrix of the micro-element.

$$\left[k^{h}\right]_{m(i)} = \int_{m(i)} [B]^{T}_{m(i)} [D]_{m(i)} [N_{\sigma}]_{m(i)} dV_{m(i)} \tag{45}$$

Both $\left[k^{el}\right]_{m(i)}$ and $\left[k^{h}\right]_{m(i)}$ are constant and inelasticity is controlled at the collocation points through the accompanying plastic strain evolution equations that in this work are of the form of Eq. (16).

Considering zero initial conditions for brevity, rates in Eq. (43) are dropped and the following relation is established

$$\left[k^{el}\right]_{m(i)} \{d\}_{m(i)} - \left[k^{h}\right]_{m(i)} \left\{\varepsilon^{pl}_{cq}\right\}_{(i)} = \{f\}_{m(i)} \tag{46}$$

Substituting Eq. (34) into Eq. (46) and pre-multiplying with $[N]^{T}_{m(i)}$ the following relation is derived:

$$\left[k^{el}\right]^{M}_{m(i)} \{d\}_{M} - \left[k^{h}\right]^{M}_{m(i)} \left\{\varepsilon^{pl}_{cq}\right\}_{(i)} = \{f\}^{M}_{m(i)} \tag{47}$$

where

$$\left[k^{el}\right]^{M}_{m(i)} = [N]^{T}_{m(i)} \left[k^{el}\right]_{m(i)} [N]_{m(i)} \tag{48}$$

is the elastic stiffness matrix of the *i*th micro-element mapped onto the macro-element degrees of freedom while $\left[k^{h}\right]^{M}_{m(i)}$ is the hysteretic matrix of the *i*th micro-element, evaluated by the following relation:

$$\left[k^{h}\right]^{M}_{m(i)} = [N]^{T}_{m(i)} \left[k^{h}\right]_{m(i)} \tag{49}$$

Finally, $\{f\}^{M}_{m(i)}$ in Eq. (47) is the equivalent nodal force vector of the micro-element mapped onto the macro-nodes of the coarse element.

$$\{f\}^{M}_{m(i)} = [N]^{T}_{m(i)} \{f\}_{m(i)} \tag{50}$$

Equation (47) is a multiscale equilibrium equation involving the displacement vector evaluated at the coarse-element nodes and the plastic part of the strain tensor evaluated at collocation points within the micro-scale element mesh.

## *4.1 Micro to Macro Scale Transition*

Having established the micro-element equilibrium in terms of macro-displacement measures using the micro-basis mapping introduced in Eq. (34), a procedure is needed to formulate the global equilibrium equations in terms of the macro-quantities.

Denoting with a subscript $M$ the corresponding macro-measures over the volume $V$ of the coarse element Eq. (37) is re-written as:

$$\int_{V_M} \{\varepsilon\}_M^T \{\dot{\sigma}\}_M dV_M = \{d\}_M^T \{\dot{f}\}_M \tag{51}$$

where $\{f\}_M$ is the vector of nodal loads imposed at the coarse element nodes. Equivalently to relation (43) the variation principle of Eq. (51) gives rise to the following equation:

$$\int_{V_M} \{\varepsilon\}_M^T \{\dot{\sigma}\}_M dV_M = [K]_{CR(j)}^M \{\dot{d}\}_M - [K^h]_{CR(j)}^M \left\{\dot{\varepsilon}_{cq}^{pl}\right\}_M \tag{52}$$

where $[K]_{CR(j)}^M$, $[K^h]_{CR(j)}^M$ are the equivalent stiffness matrix and the equivalent hysteretic matrix of the $j$th coarse element respectively. These matrices need to be expressed in terms of micro-scale measures, to account for the micro-scale effect upon the macro-scale mesh. This is accomplished by demanding that the strain energy of the coarse element is additively decomposed into the contributions of each micro-element within the coarse-element. Thus, the following relation is established:

$$\int_V \{\varepsilon\}_M^T \{\sigma\}_M dV = \sum_{i=1}^{m_{el}} \int_{V_{mi}} \{\varepsilon\}_{mi}^T \{\sigma\}_{mi} dV_i \tag{53}$$

where $\{\varepsilon\}_{mi}$, $\{\sigma\}_{mi}$ are the micro-strain and micro-stress field defined over the volume $V_{mi}$ of the $i$th micro-element. Using relations and (37), (38), the following relation is established for the r.h.s of Eq. (53)

$$\sum_{i=1}^{m_{el}} \int_{V_{mi}} \{\varepsilon\}_{mi}^T \{\sigma\}_{mi} dV_i = \sum_{i=1}^{m_{el}} \left( \{d\}_{mi}^T \left[k^{el}\right]_{m(i)} \{d\}_{m(i)} - \{d\}_{mi}^T \left[k^h\right]_{m(i)} \left\{\varepsilon_{cq}^{pl}\right\}_{m(i)} \right) \tag{54}$$

Substituting relation (47) into relation (54), the following relation is derived

$$\sum_{i=1}^{m_{el}} \int_{V_{mi}} \{\varepsilon\}_{mi}^T \{\sigma\}_{mi} dV_i = \{d\}_M^T \sum_{i=1}^{m_{el}} \left( [N]_{Mi}^T \left[k^{el}\right]_{m(i)} [N]_{Mi} \{d\}_M - [N]_{Mi}^T \left[k^h\right]_{m(i)} \left\{\varepsilon_{cq}^{pl}\right\}_{m(i)} \right) \tag{55}$$

Using Eqs. (52) and (55), Eq. (53) assumes the following form:

$$[K]_{CR(j)}^M \{d\}_M - [K^h]_{CR(j)}^M \{\varepsilon^{pl}\}_{cq} = \sum_{i=1}^{m_{el}} \left[k^{el}\right]_{m(i)}^M \{d\}_M - \sum_{i=1}^{m_{el}} \left[k^h\right]_{m(i)}^M \left\{\varepsilon_{cq}^{pl}\right\}_{m(i)} \tag{56}$$

Relation (56) holds for every compatible vector of nodal displacements $\{d\}_M$ as long as:

$$[K]^M_{CR(j)} = \sum_{i=1}^{m_{el}} [k^{el}]^M_{m(i)} \tag{57}$$

and

$$[K^h]^M_{CR(j)} \left\{ \varepsilon^{pl}_{cq} \right\} = \sum_{i=1}^{m_{el}} [k^h]^M_{m(i)} \left\{ \varepsilon^{pl}_{cq} \right\}_{m(i)} \tag{58}$$

thus, the following multiscale equilibrium equation is derived for the coarse element:

$$[K]^M_{CR(j)} \{d\}_M = \{f\}_M - \{f_h\}_M \tag{59}$$

where $\{f_h\}_M$ is a nonlinear correction to the external force vector arising from the evolution of the plastic strains within the micro-structure

$$\{f_h\}_M = \sum_{i=1}^{m_{el}} [k^h]^M_{m(i)} \left\{ \varepsilon^{pl}_{cq} \right\}_{m(i)} \tag{60}$$

while the plastic strain vectors $\{\varepsilon^{pl}_{cq}\}_{m(i)}$ are considered to evolve according to relation (16). Equations (59) and (60) are used to derive the equilibrium equation at the structural level.

## 4.2 Solution in the Macro-scale

Considering the general case of a coarse mesh with $ndof_M$ free macro-degrees of freedom and using Eq. (59), the global equilibrium equations of the composite structure can be established in the coarse mesh. In the dynamic case the following equation is established:

$$[M]\left\{\ddot{U}\right\}_M + [C]\left\{\dot{U}\right\}_M + [K]\{U\}_M = \{F\}_M + \{F_h\}_M \tag{61}$$

where $[M]$, $[C]$, $[K]$ are the ($ndof_M \times ndof_M$) macro-scale mass, viscous damping and stiffness matrix respectively. The mass matrix can be formulated following either the lamped or distributed mass approach while the viscous damping can be of either the classical or non-classical type [40]. The global stiffness matrix of the composite structure is formulated through the direct stiffness method by additively

appending the contributions of the coarse elements equivalent matrices defined in Eq. (57). The $(ndof_M \times 1)$ vector $\{U\}_M$ consists of the nodal macro-displacements.

Equation (59) expresses the nodal equilibrium of the coarse element mesh. The coarse element equivalent stiffness matrices $[K]^M_{CR(j)}$ can be assembled through the direct stiffness method to derive the stiffness matrix of the composite structure. The external load vector $\{F\}_M$ and the hysteretic load vector $\{F_h\}_M$ are assembled considering the equilibrium of the corresponding elemental contributions $\{f\}_M$ and $\{f_h\}_M$, defined in Eqs. (51) and (60) respectively, at coarse nodal points.

Equations (61) are supplemented by the evolution equations of the micro-plastic strain components defined at the collocation points within the micro-elements. These equations can be established in the following form:

$$\left\{\dot{E}^{pl}_{cq}\right\}_m = [G]\left\{\dot{\varepsilon}_{cq}\right\}_m \tag{62}$$

where the vector

$$\left\{\dot{E}^{pl}_{cq}\right\}_m = \left\{ \left\{\dot{\varepsilon}^{pl}_{cq}\right\}_{m(1)} \quad \left\{\dot{\varepsilon}^{pl}_{cq}\right\}_{m(2)} \quad \cdots \quad \left\{\dot{\varepsilon}^{pl}_{cq}\right\}_{m(m_{el})} \right\}^T \tag{63}$$

holds the plastic strain components evaluated at the collocation points of each micro-element and

$$\left\{\dot{E}_{cq}\right\}_m = \left\{ \left\{\dot{\varepsilon}_{cq}\right\}_{m(1)} \quad \left\{\dot{\varepsilon}_{cq}\right\}_{m(2)} \quad \cdots \quad \left\{\dot{\varepsilon}_{cq}\right\}_{m(m_{el})} \right\}^T \tag{64}$$

Matrix $[G]$ in relation (62) is a band diagonal matrix that assumes the following form

$$[G] = \begin{bmatrix} H_{1m(1)}H_{2m(1)}[R]_{m(1)} & & & [0] \\ & H_{1m(2)}H_{2m(2)}[R]_{m(2)} & & \\ & & \ddots & \\ [0] & & & H_{1m(m_{el})}H_{2m(m_{el})}[R]_{m(m_{el})} \end{bmatrix} \tag{65}$$

Equations (62) are independent and thus can be solved in the micro-element level resulting in an implicitly parallel scheme. Relation (65) depends on the current micro-stress state within each micro-element. The corresponding stress tensors are evaluated from the current micro-strains, using Eqs. (39) and (40).

## 5 Computational Modeling of Masonry Structures

The multiscale computational method described in Sects. 2–4 is used herein for the numerical simulation of the nonlinear dynamic response of masonry structures. In particular the use of textile composites as a means of retrofitting masonry walls is examined by comparing the nonlinear dynamic response of both plain and retrofitted specimens.

### *5.1 Natural Stone*

In this work, natural stone is considered to be an elasto-plastic isotropic material. Plasticity is introducing a Drucker-Prager [31] yield criterion and an Armstrong-Frederich (AF) [36] nonlinear kinematic hardening law in Eqs. (16) and (18) respectively.

Thus, the yield criterion $\Phi$ in Eq. (13) assumes the following form

$$\Phi = \sqrt{\frac{J_2}{2}} - c_1 J_1 \tag{66}$$

while the corresponding limit value is

$$\Phi_0 = c_2 \tag{67}$$

Parameters $c_1$ and $c_2$ in relations (66) and (67) are evaluated as

$$c_1 = \frac{\sigma_t - \sigma_c}{\sigma_t + \sigma_c} \tag{68}$$

$$c_2 = 2\frac{\sigma_t \sigma_c}{\sigma_t + \sigma_c} \tag{69}$$

where $\sigma_c$ and $\sigma_t$ are the compressive and tensile strength of the material.

To account for AF type of hardening the following relation is established for the kinematic hardening function $\{G\}_{kin}$ in Eq. (7)

$$\{G\}_{kin} = \frac{2}{3} h \frac{\partial \Phi}{\partial \{\sigma\}} - c\sqrt{\frac{2}{3}\left(\frac{\partial \Phi}{\partial \{\sigma\}}\right)^T \left(\frac{\partial \Phi}{\partial \{\sigma\}}\right)}\{\eta\} \tag{70}$$

where $h$ and $c$ are model parameters.

### 5.1.1 Numerical Experiment

The case of a uniaxial compression numerical experiment is examined. The material parameters considered are $E$ = 20.2 GPa, $\sigma_c$ = 69.2 MPa and $\sigma_t = 0.1, \sigma_c = 6.92$ MPa. The AF kinematic hardening parameters considered are $h$ = 8 GPa and $c$ = 1000. The smooth hysteretic model parameters used are $\beta = 0.1$, $\gamma = 0.9$, $N = 25$, $c_\eta$ = 0.002 and $c_s$ = 0.005. The strain envelope considered is presented in Fig. 2a. Five loading-unloading cycles are simulated. In each, the specimen is unloaded up to a value of stress $\sigma_0$ = 2.5 MPa.

In Fig. 2b the resulting stress-strain diagram is presented. In each cycle, both the strength and the unloading stiffness of the specimen is reduced due to the stiffness degradation and strength deterioration parameters introduced in relations (21) and (23) respectively. The corresponding back-stress evolution is presented in Fig. 2c. Finally, the hysteretic energy evolution is presented in Fig. 2d. In this, hysteretic energy and thus damage is accumulating even during the "elastic" unloading of the material. This is due to the effect of the stiffness degradation parameter.

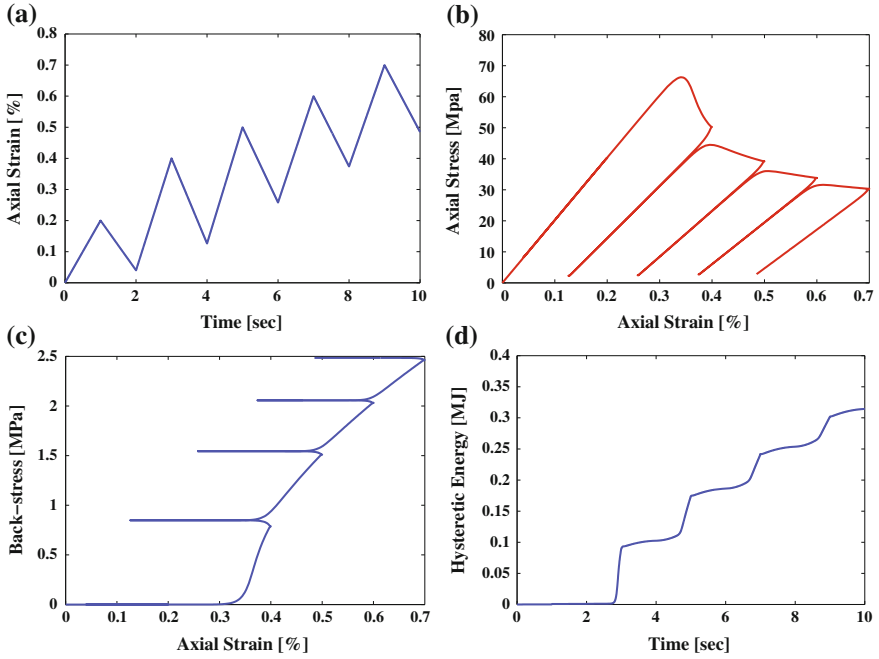


**Fig. 2** Natural stone hysteretic response. **a** Imposed strain envelope. **b** Cyclic axial stress-axial strain diagram. **c** Back-stress-axial strain diagram. **d** Hysteretic energy evolution

## 5.2 Mortar

The inelastic behaviour of mortar is modelled accordingly using a non-associative Drucker-Prager material model. Such an approach has been implemented in the past to account for the nonlinear response of concrete and cement-based materials [41]. The yield function $\Phi$ for mortar is provided from Eq. (66). However in this case the flow potential is defined as:

$$\mathscr{F} = \sqrt{3J_2} + \frac{1}{3} J_1 \tan\psi \tag{71}$$

where $J_1$, $J_2$ are the first and second invariants of the stress tensor and $\psi$ is the Drucker-Prager dilation angle. No hardening is considered for the mortar material.

### 5.2.1 Numerical Experiment

A uniaxial compression-tension numerical experiment is considered in this case. The model parameters are $E$ = 3494 MPa, $\sigma_c$ = 3 MPa, $\sigma_t$ = 0.3 MPa, $\psi = 60^0$ $\beta = \gamma = 0.5$, $N = 2$, $c_\eta = 0.002$ and $c_s = 0.05$. Furthermore, the following pinching parameters are considered namely $\zeta_1^0 = 1.0$, $\psi_0 = 0.05$, $\delta_\psi = 0.01$, $\mu = 0.0001$, $p = 1.2$ and $q = 0.0001$.

The imposed strain envelope is $\varepsilon = 0.0005t/10\sin(\pi t)$ (Fig. 3a). The evolution of the hysteretic energy accumulating per cycle is presented in Fig. 3b. Compared to Fig. 2d, the chosen set of parameters results in higher accumulation rates. The resulting stress-strain diagram is presented in Fig. 3c. Last, the evolution of the pinching parameter is shown in Fig. 4d. The pinching parameter assumes decreasing values only within a region of elastic loading. However the aboslute value of the pinching parameter increases as damage accumulates.

## 5.3 Textile Composite Reinforcement

To accurately predict the nonlinear behaviour of the composite an anisotropic yield criterion is required such as the Tsai-Wu failure surface introduced in [42]. However anisotropic yield and failure surfaces need extensive experimental investigation for the calibration of the corresponding material parameters where combined stress-states need to be considered. Based on the experimental data provided, a two-parameter yield surface can be calibrated. Thus the pressure-dependent Drucker-Prager yield surface defined in Eq. (66) is also implemented for the textile composite material. The Drucker-Prager yield surface has been implemented and validated in various applications of fibre and textile reinforced composites [43, 44].

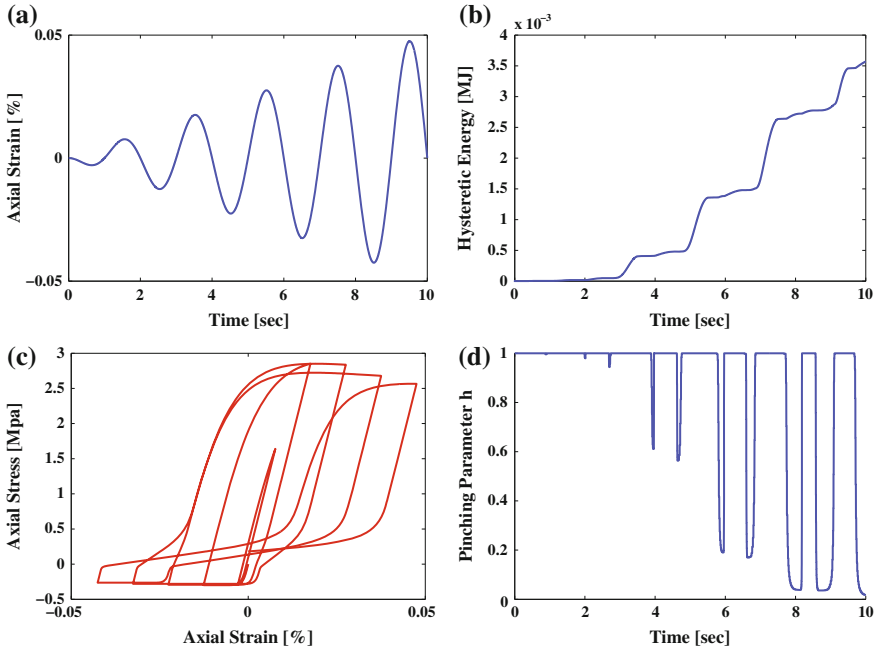


**Fig. 3** Mortar hysteretic response. **a** Imposed strain envelope. **b** Hysteretic energy evolution. **c** Cyclic axial stress-axial strain diagram. **d** Pinching parameter evolution

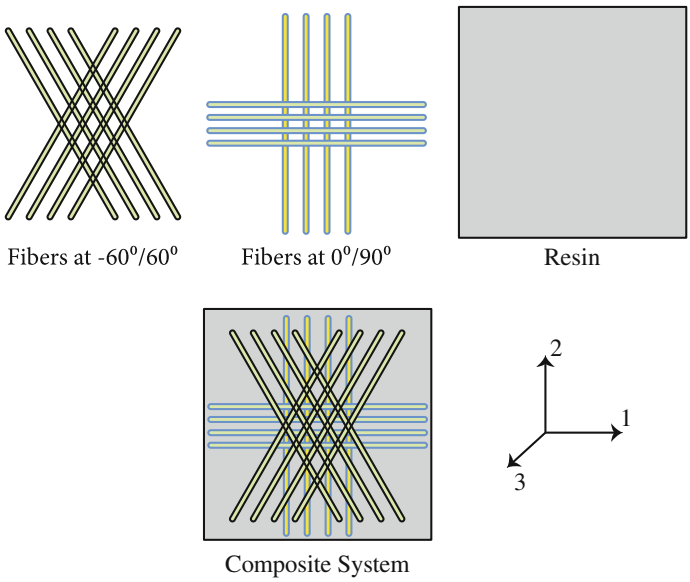


**Fig. 4** Textile composite layers and local axes

**Table 1** Textile composite elastic properties

| Young's modulus (MPa) | | | | | |
|---|---|---|---|---|---|
| $E_{11}$ | $E_{22}$ | $E_{22}$ | $E_{12}$ | $E_{23}$ | $E_{13}$ |
| 40,000 | 32,000 | 32,000 | 4500 | 4500 | 4500 |
| Poisson's ratio | | | | | |
| $\nu_{12}$ | | $\nu_{23}$ | | $\nu_{13}$ | |
| 0.14 | | 0.2 | | 0.2 | |

No hardening is considered in this case. A homogenized anisotropic material constitutive model is considered for the textile reinforced composite as suggested in [12]. The elastic properties of the homogenized material are presented in Table 1.

The orientation of the local element axes 11, 22, 33 for the homogenized material are presented in Fig. 4. The shear and tensile strengths of the wrap-knitted fibers are considered to be to be equal to $\sigma_t = 10$ MPa and $\sigma_t = 400$ MPa respectively [12]. Furthermore, the compressive strength of the cement-based mortar used as the matrix of the textile composite material is $\sigma_c = 30$ MPa [45] (Fig. 4).

The hysteretic and damage related parameters are $\beta = 0.5$, $\gamma = 0.5$, $N = 25$, $c_\eta = 0.002$ and $c_s = 0.005$.

## 6 Numerical Applications

The cantilever masonry wall presented in Fig. 5 is considered, consisting of stone blocks, bonding mortar and an outer layer of textile component reinforcement is considered. The material properties for the stone, mortar and reinforcement have been introduced in Sects. 5.1, 5.2 and 5.3 respectively. The wall is considered to be laterally supported. A mass $m = 20$ tn is considered at the top of the wall. The densities of the constituent materials are $\rho_s = 1.8$ tn/m$^3$, $\rho_m = 1.2$ tn/m$^3$ and $\rho_t = 2.0$ tn/m$^3$ for the natural stone, mortar and textile composite layer respectively. No viscous damping has been considered in this example.

A series of time-history analyses is performed using the HHT method [46] to integrate the equations of motion. The corresponding numerical dissipation coefficient is set to $\alpha_{HHT} = -0.1$. A constant time step equal to $dt = 0.001$ s is considered in all cases. Results are derived at constant time step equal to $dt_{out} = 0.005$ s. All analyses were performed in a personal computer fitted with an Intel Core-i7 CPU and 8 GB of RAM.

The two models (URMW and RMW) are subjected to a series of seven pairs of unscaled ground motion records derived from the PEER database [47]. The ground-motion records considered together with their corresponding peak values are presented in Table 2.

The corresponding time-histories are presented in Fig. 6a, b for the fault-normal and fault-parallel direction of excitation respectively.

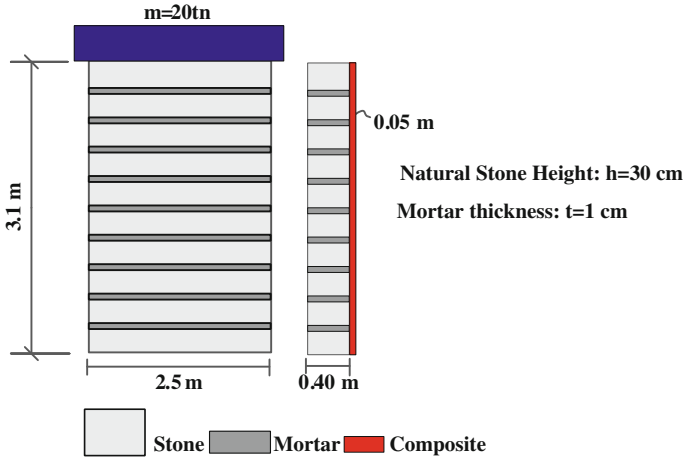


**Fig. 5** Textile composite reinforced stone masonry wall

**Table 2** Ground motion records

| Ground motion record | NGA index | PGA | |
|---|---|---|---|
| (–) | (–) | Fault normal (g) | Fault parallel (g) |
| Friuli, 1976 | #130 | 0.09 | 0.11 |
| Victoria-Mexico, 1980 | #266 | 0.15 | 0.09 |
| Northridge, 1995 | #957 | 0.12 | 0.16 |
| Imperial Valley(E06), 1979 | #185 | 0.25 | 0.22 |
| Chi-Chi, 1999 | #1201 | 0.25 | 0.31 |
| Imperial Valley(E07), 1979 | #205 | 0.19 | 0.13 |
| Coyote Lake, 1979 | #145 | 0.28 | 0.16 |

The corresponding Response Spectra (RS) are presented in Fig. 7a, b respectively. The provided RS are compared with the elastic spectrum defined in EC8 [48] considering a ground acceleration $\alpha_g = 0.16g$, soil factor $S = 1.2$, corner periods $\{T_B, T_C, T_D\} = \{0.15, 0.5, 2.5\}$ and 5 % damping.

In all the analysis cases considered, the ground motion record with the highest PGA is imposed on the longitudinal direction of the wall.

## *6.1 Verification*

For verification purposes, a set of analysis cases is performed where the effect of damage (i.e. setting $c_\eta = 0.0$, $c_s = 0.0$ and $\zeta = 0.0$ for the stiffness degradation, strength deterioration and pinching parameters respectively. The derived results are compared to the results obtained from a conventional finite element model using the

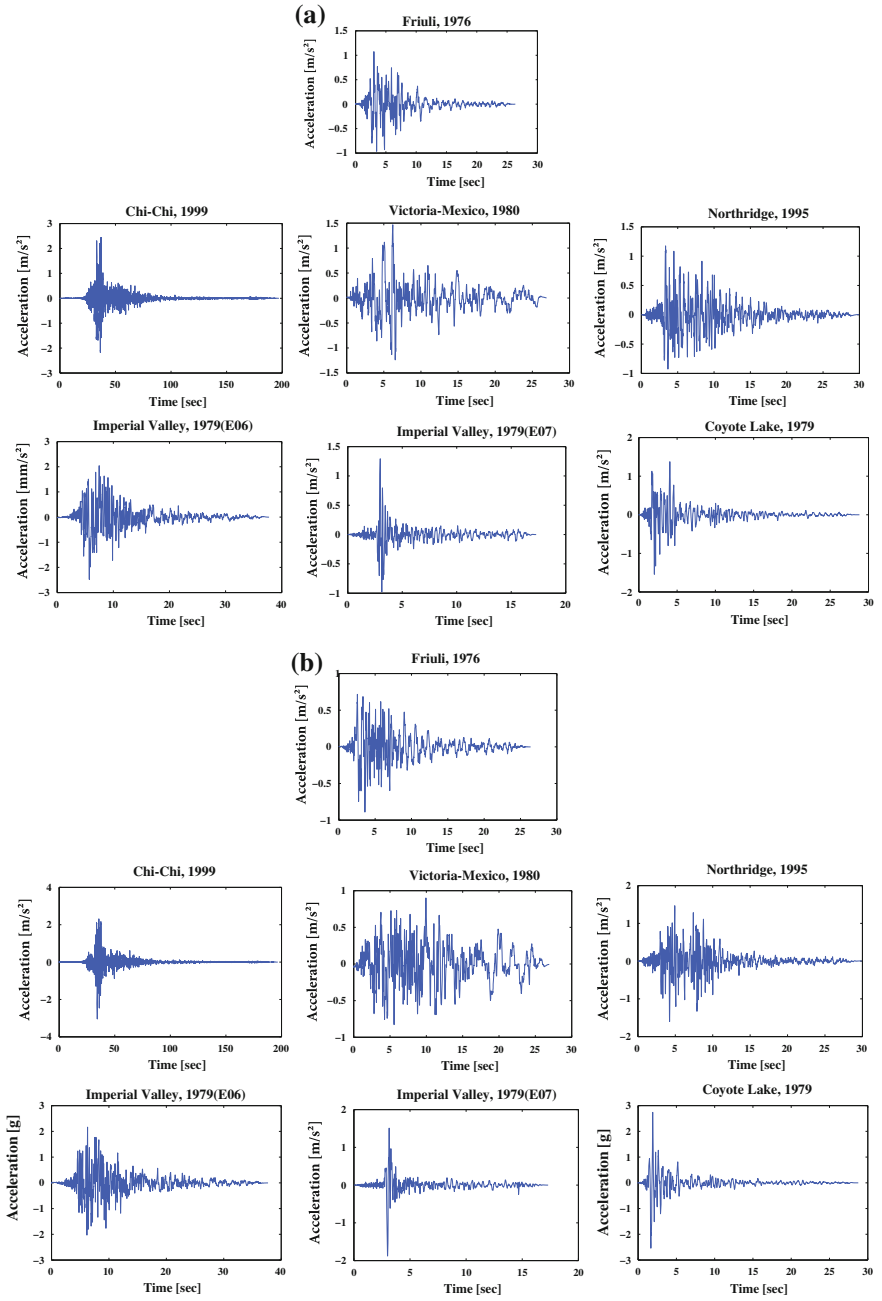


**Fig. 6** Ground motion records. **a** Fault-parallel components. **b** Fault-normal components

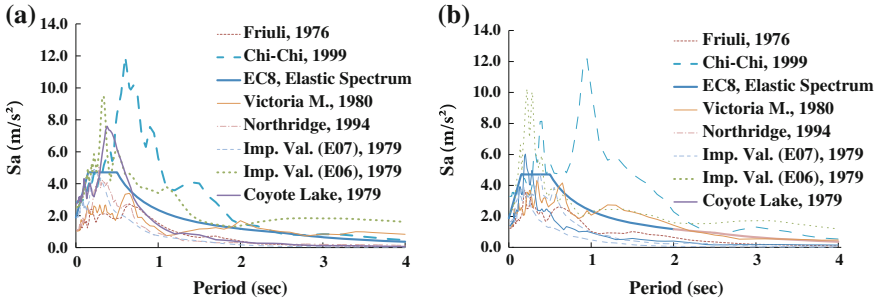


**Fig. 7** Ground acceleration record response spectra. **a** Fault normal. **b** Fault parallel

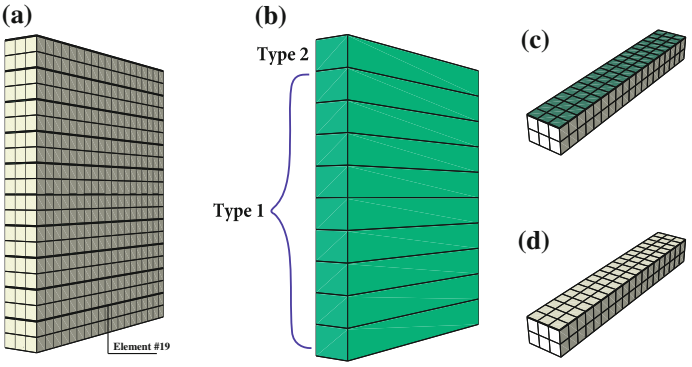


**Fig. 8** **a** Finite element model. **b** Multiscale model—coarse mesh. **c** Multiscale model coarse element type #1. **d** Multiscale model coarse element type #2

Abaqus commercial code [49]. Material nonlinearity in Abaqus is treated using the Full Newton-Raphson method [35]. The C3D8 hex-element with full integration [49] is implemented in both cases. The finite element mesh consists of 1710 elements and 2484 nodes (Fig. 8a). The multiscale element consists of 10 coarse elements and 44 nodes. Each coarse element consists of 171 micro-elements (Fig. 8c, d). Two types of coarse elements are considered since the coarse element at the top of the wall does not have a mortar layer. The distribution of coarse elements is presented in Fig. 8b). The oscillatory boundary condition assumption is used for the evaluation of the micro to macro numerical mapping.

The free end displacement time-history components derived from the Victoria-Mexico analysis case are presented in Figs. 9 and 10 for the in-plane and the out-of-plane component respectively. The first 15 s of the derived time-history are presented for clarity. The results obtained from the two different methodologies are in good agreement. The differences observed, especially in the high frequency oscillations after the 10th second, are attributed to the numerical assumptions governing the evaluation of the effective stiffness of the coarse element that also

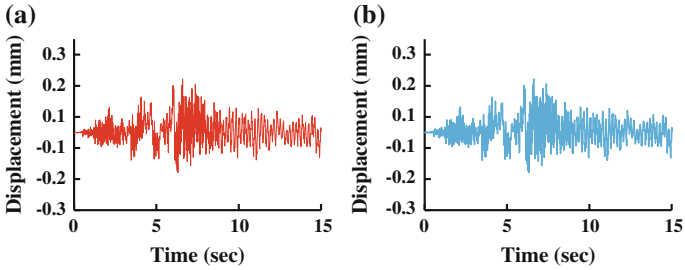


**Fig. 9** Top layer out-of-plane displacement component. **a** Abaqus. **b** Multiscale formulation

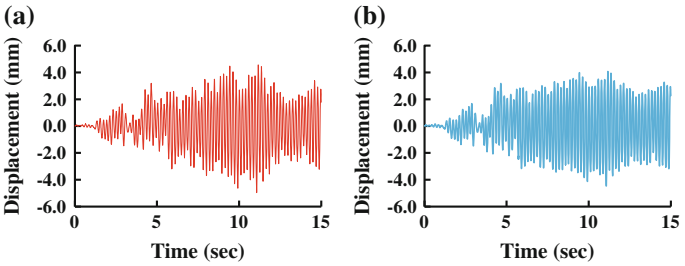


**Fig. 10** Top layer longitudinal displacement component. **a** Abaqus. **b** Multiscale formulation

affect the derived mass matrix. Thus, small variations in the computational eigenfrequencies of the multi-scale model as compared to the finite element one are expected (Fig. 8).

The required computational time for the FEM analysis model was approximately 125 min while the corresponding time for the multiscale model 14 min. The reduction in the computational time is approximately 88 %.

## *6.2 Unreinforced Masonry Wall*

Next, the URMW multiscale model is analyzed for all the ground motion records defined in Table 2 considering both plasticity and damage evolution. The corresponding parameters for the evolution of stiffness degradation, damage deterioration and pinching are defined in Sects. 5.1.1 and 5.2.1 for the natural stone and mortar respectively.

The derived free-end displacement time-histories are presented in Figs. 11 and 12 for the longitudinal and out-of-plane displacement component respectively.

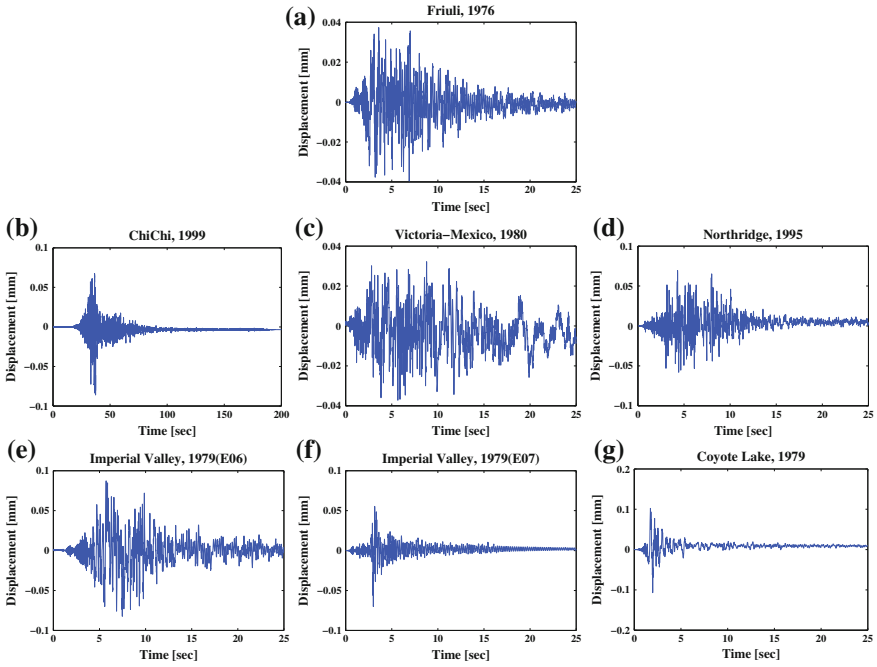


**Fig. 11** URMW—free end longitudinal displacement time histories

In all cases plastic deformation and therefore damage accumulates on the mortar joints of the masonry wall. In Fig. 13, the evolution of the hysteretic energy accumulated in the lower mortar layer is presented. The five most significant out of the seven analysis cases are presented in the plot for clarity. The Friuli and Imperial Valley(E06) records result in the highest damage intensities. This conclusion can also be verified by comparing their spectral content against the out-of-plane eigen-period of the wall ($T = 1.19$ s). In almost all of the examined cases, the mortar layer assumes its maximum damage intensity at an extremely high rate. The Victoria-Mexico event however results in a gradual increase of the accumulated hysteretic energy.

In Fig. 14a typical stress-strain hysteresis loop is presented retrieved at the Gauss point #1 of micro-element #19 located at the midspan of the lower mortar layer (Fig. 8a). Due to the relatively large thickness of the mortar layer in this model the mortar joints fail due to tensile rather than shear action. The effect of the strength deterioration parameter on the material response is evident in Fig. 8b where the stress path of the same Gauss point is presented in the $p$, $q$ space where $p$ is the hydrostatic component of the stress tensor and $q = \sqrt{\frac{3}{2}\{s\}^T\{s\}}$ while $\{s\}$ is the deviatoric part of the stress tensor. In the $pq$ space, the initial yield surface defined by the Drucker-Prager criterion is represented by a straight line. After the initial

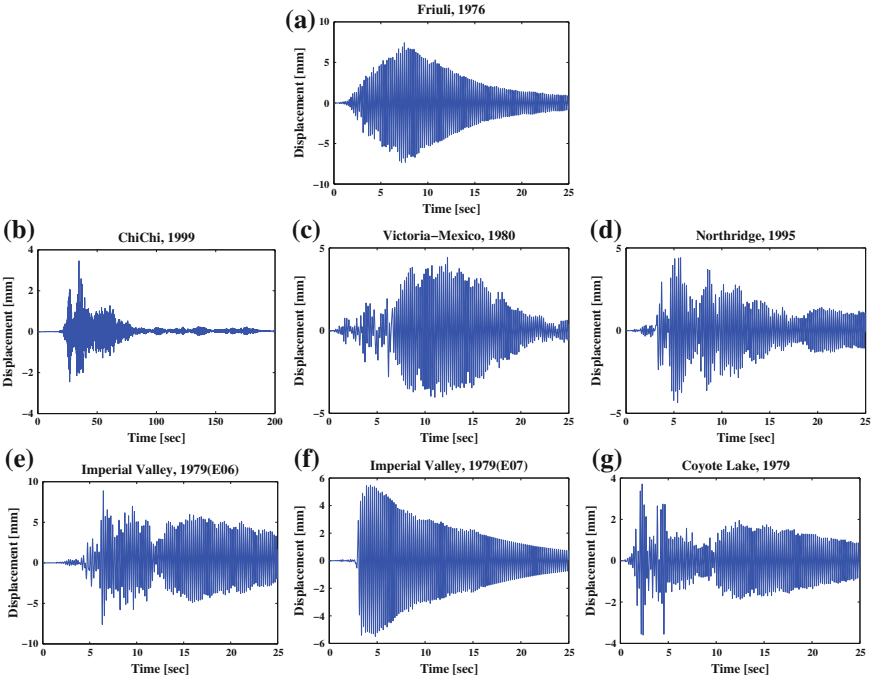


**Fig. 12** URMW—free end out of plane displacement time histories

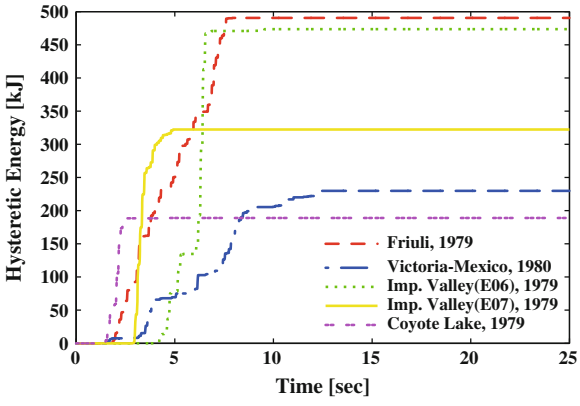


**Fig. 13** Hysteretic energy accumulation at the bottom mortar layer-unreinforced wall

yielding of the material point the slope of the line gradually decreases as predicted by Eqs. (23) and (11).

The required computational time for both the analysis and the output manipulation for the seven analysis cases was approximately 157 min.

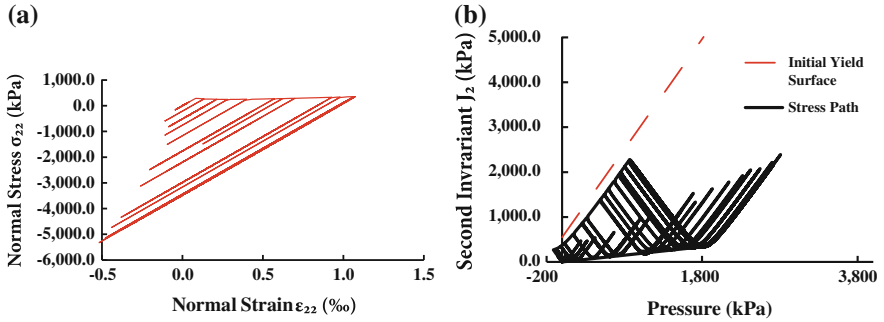


**Fig. 14** **a** Stress-strain hysteresis loop of mortar element. **b** Corresponding stress path

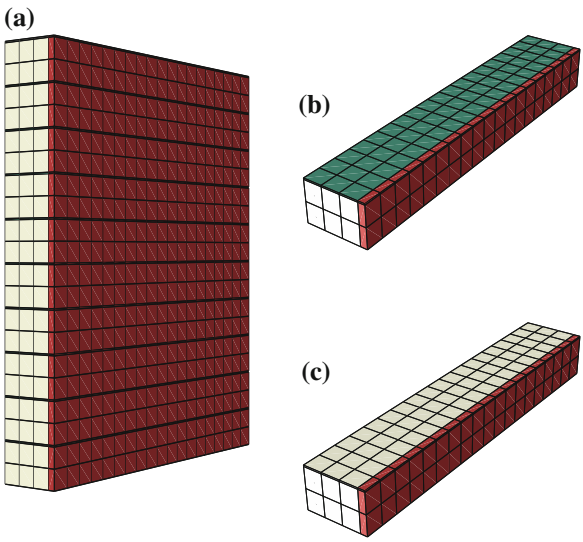


**Fig. 15** **a** Finite element model. **b** Multiscale model coarse element #1. **c** Multiscale model coarse element #2

## *6.3 Textile Composite Retrofitted Masonry Wall*

In this case, a single layer of textile composite reinforcement is added on the masonry wall. The homogenized properties defined in Sect. 5.3 are considered. The fine-meshed finite element model presented in Fig. 15a consists of 2223 hex-elements and 3020 nodes. The multiscale model again consists of 10 coarse elements and 44 nodes. Two types of coarse elements are defined each one consisting of 228 micro-elements (Fig. 15b, c). The eigen-periods of the structure under consideration are $T_{in}$ = 0.19 s and $T_{out}$ = 0.91 s for the in-plane and out-of-plane eigen modes respectively. Thus, the first four ground motion records (Table 2) represent the case of extreme seismic incidents where the performance level of Near

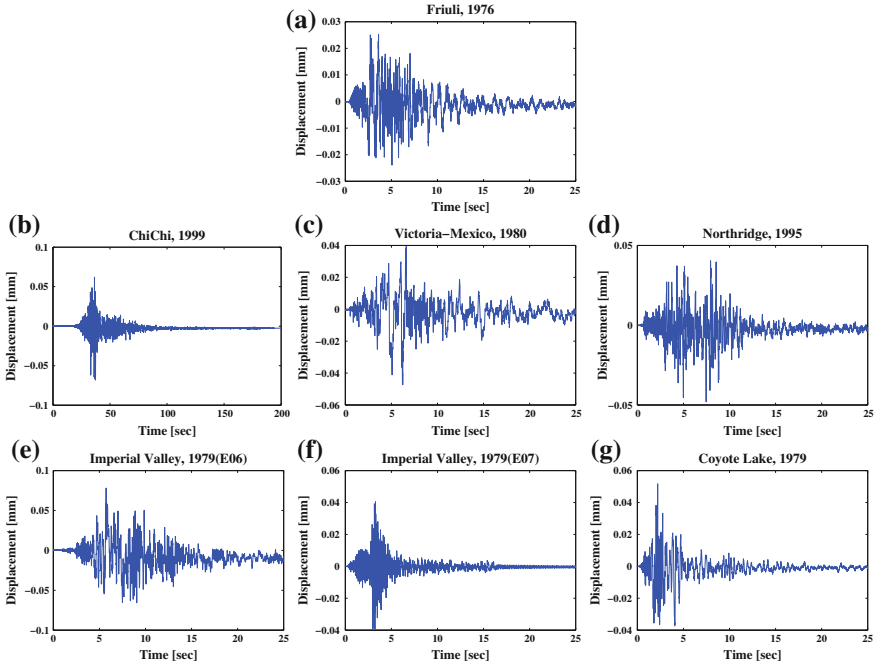


**Fig. 16** RMW—free end longitudinal displacement time histories

Collapse(EC8) needs to be achieved while for the rest a performance level of limited damage should be achieved.

The derived results in terms of free end displacement time-histories are presented in Figs. 16 and 17 for the longitudinal and out-of-plane displacement components respectively. Compared to the URMW case, the peak displacements are clearly reduced due to the increased stiffness provided from the textile composite layer. The maxima of the displacement time-histories for the two cases (URMW and RMW) are presented in Table 3. In most cases, the reduction in the absolute value if the out-of-plane maximum displacement of the order of 50 %. This reduction is even larger in the Northridge and Imperial Valley(E07) case where the increased stiffness shifts the eigen-period of the wall away from the high spectral acceleration region of the corresponding response spectra.

Although the reduction in displacement terms is significant, damage accumulation is not avoided. However both the absolute value and the rate of damage accumulation, as depicted in the corresponding hysteretic energy plot of the bottom mortar layer is significantly reduced. Thus, although the textile composite layer succeeds in increasing the overall strength and stiffness of the masonry wall, only

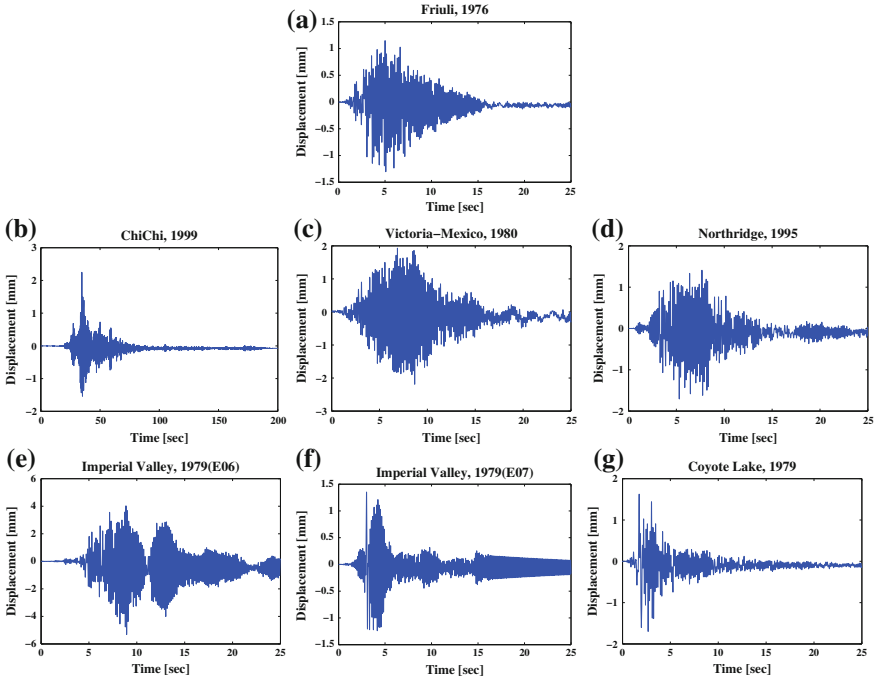


**Fig. 17** RMW—free end out of plane displacement time histories

**Table 3** Maxima of displacement components

| Ground motion record | Displacement | | | |
|---|---|---|---|---|
| | Longitudinal (mm) | | Out-of-plane (mm) | |
| | URMW | RMW | URMW | RMW |
| Friuli, 1976 | 0.04 | 0.03 | 4.43 | 2.19 |
| Victoria-Mexico, 1980 | 0.05 | 0.04 | 4.43 | 2.19 |
| Northridge, 1995 | 0.07 | 0.05 | 4.40 | 1.70 |
| Imperial Valley(E06), 1979 | 0.09 | 0.08 | 8.88 | 5.32 |
| Chi-Chi, 1999 | 0.09 | 0.07 | 3.45 | 2.25 |
| Imperial Valley(E07), 1979 | 0.07 | 0.04 | 5.49 | 1.35 |
| Coyote Lake, 1979 | 0.11 | 0.05 | 3.71 | 1.70 |

by slightly altering its initial thickness, it needs to be combined with conventional measures to provide acceptable retrofit solutions at the Damage Limitation performance level (Fig. 18).

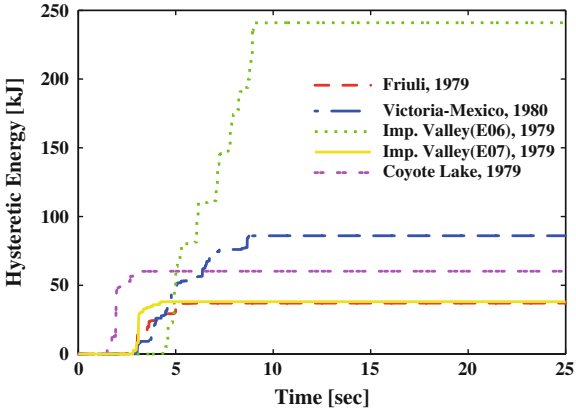


**Fig. 18** Hysteretic energy accumulation at the bottom mortar layer-retrofitted wall

## 7 Conclusions

The nonlinear dynamic analysis of heterogeneous structures can be an arduous and time-consuming procedure. However, it provides significant insight on the dynamics of the structural response and provides a reliable on the inelastic processes undergoing at the material level. In this work a multiscale analysis procedure, namely the hysteretic multiscale finite element scheme, is considered for the computational up-scaling of refined finite element problems. Using this method, the response of a natural stone masonry wall is examined under seismic excitation. Next, a layer of textile composite reinforcement is added onto the assembly and the response of the strengthened structure is examined. From the computational perspective, the multiscale method used enables the engineer to run a series of analysis models in an affordable amount of time. In terms of modeling efficiency, the multiscale model together with the hysteretic model adopted manage to capture the dynamics of the structure under consideration. The textile composite reinforcement layer increases the stiffness of the masonry wall, while at the same time the accumulated damage, quantified through an energy measure decreases. Future research will focus on the incorporation of brittle cracking mechanisms within the presented multi-scale formulation to further enhance the versatility of the method and provide more accurate estimates for the dynamic response of brittle structures.

**Acknowledgments** This work has been carried out under the support of the Swiss National Science Foundation for Research Grant #200021_146996: “Hysteretic Multi/Scale Modeling for the Reinforcing of Masonry Structures”.

## References


1. Chesi C, Binda L, Parisi MA (2010) Seismic damage to churches: Observations from the L'Aquila, Italy, earthquake and considerations on a case-study. *Advanced Materials Research*, 133–134:641–646
2. Dizhur D, Ingham J, Moon L, Griffith M, Schultz A, Senaldi I, Magenes G, Dickie J, Lissel S, Centeno J, Ventura C, Leite J, Lourenco P (2011) Performance of masonry buildings and churches in the 22 February 2011 Christchurch earthquake. Bull NZ Soc Earthq Eng 44 (4):279–296
3. Binda L, Gatti G, Mangano G, Poggi C, Sacchi LG (1992) The collapse of the civic tower of Pavia: a survey of the materials and structure. Mason Int 6:11–20
4. Verstrynge E, Schueremans L, Van Gemert D, Wevers M (2009) Monitoring and predicting masonry's creep failure with the acoustic emission technique. NDT E Int 42(6):518–523
5. ElGawady M, Lestuzzi P, Badoux M (2005) In-plane seismic response of URM walls upgraded with FRP. J Compos Constr 9(6):524–535
6. Habel K, Denarié E, Brühwiler E (2006) Structural response of elements combining ultrahigh-performance fiber-reinforced concretes and reinforced concrete. J Struct Eng 132(11):1793–1800
7. POLYMAST (2011) polyfunctional technical textiles for the protection and monitoring of masonry structures against earthquakes, final report, seventh framework programme capacities specific programme research infrastructures, project no.: 227887. http://www.series.upatras.gr/polymast
8. Antonopoulos C, Triantafillou T (2003) Experimental investigation of FRP-strengthened RC beam-column joints. J Compos Constr 7(1):39–49
9. Sivaraja SS, Thandavamoorthy TS, Vijayakumar S, Aranganathan SM, Dasarathy AK (2013) Preservation of historical monumental structures using fibre reinforced polymer (frp)—case studies. Procedia Eng 54(0):472–479. The 2nd international conference on rehabilitation and maintenance in civil engineering (ICRMCE)
10. Triantafillou TC, Fardis MN (1997) Strengthening of historic masonry structures with composite materials. Mater Struct 30(8):486–496
11. Messervey TB, Zangani D, Fuggini C (2013) Sensor embedded textiles for the reinforcement, dynamic characterisation, and structural health monitoring of masonry structures. In: Proceedings of the 5th EWSHM 2010, Sorrento, Italy, June 28–July 2, pp 1075–1082
12. Fuggini C, Chatzi E, Zangani D (2013) Combining genetic algorithms with a meso-scale approach for system identification of a smart polymeric textile. Comput Aided Civil Infrastruct Eng 28(3):227–245
13. Krebber K, Liehr S, Witt J (2012) Smart technical textiles based on fibre optic sensors. In: Proceedings of SPIE 8421, OFS2012 22nd international conference on optical fiber sensors
14. Thomas K (1996) Masonry walls: specification and design. Butterworth Heinemann, Oxford
15. Morton J, Haig G (2011) Designers' guide to Eurocode 6: design of masonry structures: EN 1996-1-1: general rules for reinforced and unreinforced masonry. ICE Publishing, London
16. Binda L, Pina-Henriques J, Anzani A, Fontana A, Lourenco PB (2006) A contribution for the understanding of load-transfer mechanisms in multi-leaf masonry walls: testing and modeling. Eng Struct 28:1132–1148
17. BS EN 1998-3 (2005) Eurocode 8: design of structures for earthquake resistance. Assessment and retrofitting of buildings
18. American Society of Civil Engineers (2007) Seismic rehabilitation of existing buildings (41-06). American Society of Civil Engineers
19. Fardis M (2010) Advances in performance-based earthquake engineering. Springer, Berlin
20. Massart TJ, Peerlings RHJ, Geers MGD (2004) Mesoscopic modeling of failure and damage-induced anisotropy in brick masonry. Eur J Mech A Solids 72(8):1022–1059
21. Mojsilovic' N (2011) Strength of masonry subjected to in-plane loading: a contribution. Int J Solids Struct 48(6):865–873

22. Lourenc'o P (1996) Computational strategies for masonry structures. In: PhD thesis, Delft University of Technology, The Netherlands
23. Anthoine A (1992) In-plane behaviour of masonry: a literature review. Report EUR 13840 EN, commission of the European communities. Technical report, JRC—Institute for Safety Technology, Ispra, Italy
24. Chen S-Y, Moon FL, Yi T (2008) A macroelement for the nonlinear analysis of in-plane unreinforced masonry piers. Eng Struct 30(8):2242–2252
25. Peerlings RHJ, Geers MGD, Massart TJ (2007) An enhanced multiscale approach for masonry wall computations with localization of damage. Int J Numer Methods Eng 69(5):1022–1059
26. Massart TJ, Peerlings RHJ, Geers MGD, Gottcheiner S (2005) Mesoscopic modeling of failure in brick masonry accounting for three-dimensional effects. Eng Fract Mech 72(8):1238–1253
27. Efendiev Y, Hou TY (2009) Multiscale finite element methods. Surveys and tutorials in the applied mathematical sciences, vol 4. Springer, New York
28. Zhang HW, Wu JK, Lv J (2012) A new multiscale computational method for elasto-plastic analysis of heterogeneous materials. Comput Mech 49(2):149–169
29. Triantafyllou SP, Chatzi EN (2014) A hysteretic multiscale formulation for nonlinear dynamic analysis of composite materials. Comput Mech 54(3):763–787
30. Triantafyllou S, Koumousis V (2014) Hysteretic finite elements for the nonlinear static and dynamic analysis of structures. J Eng Mech 140(6):04014025
31. Lubliner J (2008) Plasticity theory. Dover Publications, New York
32. Nemat-Naser S (1982) On finite deformation elasto-plasticity. Int J Solids Struct 18 (10):857–872
33. Erlicher S, Bursi O (2008) Bouc-wen type models with stiffness degradation: thermodynamic analysis and applications. J Eng Mech 134(10):843–855
34. Foliente GC, Singh MP, Noori MN (1996) Equivalent linearization of generally pinching hysteretic and degrading systems. Earthq Eng Struct Dyn 25:611–629
35. Zienkiewicz OC, Taylor RL, Zhu JZ (2005) The finite element method: its basis and fundamentals, 6th edn. Elsevier, Amsterdam
36. Armstrong PJ, Frederick CO (1966) A mathematical representation of the multiaxial Bauschinger effect. Technical report, report RD/B/N 731 central electricity generating board
37. Belytschko T, Lu YY, Gu L (1994) Element-free Galerkin methods. Int J Numer Methods Eng 37(2):229–256
38. Triantafyllou SP, Koumousis VK (2012) A hysteretic quadrilateral plane stress element. Arch Appl Mech 82(10–11):1675–1687
39. Washizu K (1983) Variational methods in elasticity and plasticity. Pergamon Press, Oxford
40. Chopra A (2006) Dynamics of structures. Prentice Hall, New York
41. Wu C, Hao H (2006) Derivation of 3d masonry properties using numerical homogenization technique. Int J Numer Methods Eng 66(11):1717–1737
42. Tsai SW, Wu EM (1971) A general a general theory of strength for anisotropic materials. J Compos Mater 5:58–80
43. Flores S, Evans AG, Zok FW, Genet M, Cox B, Marshall D, Sudre O, Yang Q (2010) Treating matrix nonlinearity in the binary model formulation for 3d ceramic composite structures. Compos A: Appl Sci Manuf 41(2):222–229
44. Jiang J-F, Wu Y-F (2012) Identification of material parameters for drucker-prager plasticity model for FRP confined circular concrete columns. Int J Solids Struct 49(3â€“4):445–456
45. Papanicolaou CG, Triantafillou TC, Karlos K, Papathanasiou M (2007) Textile-reinforced mortar (TRM) versus FRP as strengthening material of URM walls: in-plane cyclic loading. Mater Struct 40(10):1081–1097
46. Hilber HM, Hughes TJR, Taylor RL (1977) Improved numerical dissipation for time integration algorithms in structural dynamics. Earthq Eng Struct Dyn 5(3):283–292
47. http://peer.berkeley.edu/peer_ground_motion_database/. Accessed 20 May 2014
48. BS EN 1998-1 (2004) Eurocode 8: design of structures for earthquake resistance—Part 1: general rules seismic actions and rules for buildings
49. Abaqus version 6.11 [Computer software]. Dassault Systmes Simulia, Providence, RI